Journal of Materials Chemistry A

High-Efficiency Frost and Ice Control *via* Sensing-Assisted Nanovibrational Slippery Surfaces

Journal:	*Journal of Materials Chemistry A*
Manuscript ID	TA-ART-03-2025-002324.R1
Article Type:	Paper
Date Submitted by the Author:	22-Apr-2025
Complete List of Authors:	SHEN, YUCHEN; The University of Texas at Dallas, Boylan, Dylan; The University of Texas at Dallas Chen, Fangying; The University of Texas at Dallas Guo, Feng; Indiana University Bloomington, Intelligent Systems Engineering He, Meiying; The University of Texas at Dallas Dai, Xianming; The University of Texas at Dallas, Mechanical Engineering

High-Efficiency Frost and Ice Control *via* Sensing-Assisted Nanovibrational Slippery Surfaces

Yuchen Shen[1†], Dylan Boylan[1†], Fangying Chen[1†], Feng Guo[2], Meiying He[1], Xianming Dai[1*]

[1]Department of Mechanical Engineering, University of Texas at Dallas, 800 W Campbell Rd, Richardson, TX 75080

[2]Department of Intelligent Systems Engineering, Indiana University Bloomington, 107 S Indiana Ave, Bloomington, IN 47405

[†]These authors contributed equally to this work

*Corresponding Author: Dai@utdallas.edu

Abstract

Frost and ice accretions on surfaces pose persistent challenges across numerous industrial, residential and transportation systems. While various removal strategies exist, they often suffer from limited effectiveness or high energy consumption, such as frosting delay, ice crack generation, and Joule heating. Here, we report a novel integrated approach combining vibrational quasi-liquid surface (QLS) and capacitive sensing for efficient condensate, frost, and ice management. Compared to Joule heating, our approach does not rely on complete melting and evaporation for removal, resulting in 68% and 95% energy savings for frost and ice removal, respectively. Our QLS coating significantly reduces surface retention forces, achieving 91% and 87% less residual mass compared to hydrophilic surfaces for frost and ice removal through surface nanovibration, respectively. The integrated capacitive sensor provides real-time detection of different phase states, enabling on-demand removal in precise timeframes. This sensor-assisted approach showed 3.8 times lower energy consumption compared to conventional Joule heating for defrosting. This synergistic integration of surface engineering, nanovibration, and intelligent sensing represents a significant advancement in phase change processes, offering an energy-efficient solution for frost and ice mitigation in energy-intensive systems.

Supplementary Information, including one PDF document and seven video files, is available.

Introduction

Frost and ice accretions pose significant challenges across a broad range of industrial fields, such as air conditioning and heat pumps[1, 2], cryostorages[3], vehicles[4], power lines[5], and aerospace systems[6], leading to poor energy efficiencies[7], substantial performance degradation[8, 9], and potential system failures[10, 11]. Current approaches to frost and ice removal face significant challenges across two primary strategies: passive and active techniques. Passive approaches have explored promising surface modifications to mitigate condensate accumulations, thereby breaking the pathway for subsequent ice or frost formation[12, 13]. For instance, superhydrophobic surfaces with nano- and micro-structural designs exhibit extreme water-repellent properties[14-16], while facing significant challenges in maintaining long-term performance and durability in practical applications[17]. These surfaces are particularly vulnerable to frost and ice formation as the air layer can be displaced in humid conditions, and their delicate micro/nanostructures could degrade under mechanical wear during ice removal[17]. Thus, slippery liquid-infused surfaces offer another approach for lubricant retention but need additional effort to retain the lubricating layer under varying conditions[18-20]. The effectiveness of these surfaces can be compromised during frost/ice removal as the lubricant may be depleted or displaced by mechanical forces, requiring frequent and often challenging lubricant replenishment[21, 22]. By using chemical bonding but not structural entrapment (*e.g.*, micro/nano-textured surfaces), quasi-liquid surface(s) (QLS) can provide a more durable and scalable passive approach[23, 24]. In addition, interfacial cracks can be generated to reduce ice adhesion on durable surfaces[25-27]. However, these passive techniques rely on gravity for frost and ice removal, resulting in failure on horizontal surfaces. Therefore, active frost and ice removal techniques are needed on horizontal surfaces. Heating-based techniques, such as pulse heating and external heaters[28-30], apply high-intensity thermal energy to melt the interfacial layer. At the system level, reverse cycle and hot gas bypass defrosting are widely used in heat pumps and air conditioning systems[29, 31, 32], where the internal heat from the refrigerant is used for frost removal. Nevertheless, these methods typically consume a large amount of energy, often reaching 10-30% of the total energy capacity of the system[33]. Eco-friendly methods, including infrared and solar-assisted heating removal[34-36], offer alternatives while struggling to be reliable in environments with limited solar/infrared energy availability, such as cold-climate heat pumps.

Surface vibration has emerged as an innovative approach to defrosting and deicing, bringing several advantages over traditional techniques. In recent decades, various vibration strategies have

Supplementary Information, including one PDF document and seven video files, is available.

been explored, including piezoelectric actuators[37], electromagnetic[38] and electrostatic systems[39]. While these approaches have demonstrated some success for deicing, they face significant limitations in energy efficiency, spatial control, and operational complexity[40]. In contrast, surface acoustic waves (SAW) represent an effective approach for condensation, frost and ice removal, offering control and efficiency through high-frequency mechanical waves that propagate along material surfaces[41, 42]. Operating at high frequencies[43], SAW generates stronger streaming forces and radiation pressure in fluid while requiring lower power input compared to conventional methods[44, 45]. However, surface vibration faces a fundamental challenge in frost and ice removal applications. Specifically, the removal forces generated by these vibration-based methods are insufficient to overcome the adhesive interactions between ice/frost and the substrate[24, 46], rendering them ineffective for frost and ice removal regardless of the operating conditions. This highlights the need for integrating ultralow adhesion surface treatments with surface vibration. For instance, QLS offers exceptionally low surface retention forces and maintains stable slippery properties during vibration, making them ideal candidates for enhancing vibration-based removal. Yet, this synergistic combination of QLS with nanovibration remains unexplored in current literature, presenting a significant opportunity in the field of advanced defrosting and deicing technologies.

Furthermore, energy efficiency remains critical for industrial defrosting and deicing applications. To address this challenge, sensing technologies have been developed to enable on-demand activation of defrosting and deicing systems, such as microwave sensors and acoustic wave sensors for ice detection[47, 48], pressure transducers, thermocouples and piezoelectric sensors for indirect frost detection[49-51]. Optical fiber sensors and impedance-based direct detection systems have also been explored for frost and ice monitoring but are limited by cost, complexity, and environmental sensitivity[52, 53]. On the other hand, capacitive sensing has gained attention as a particularly effective method for detecting different phases of water, as these sensors can distinguish between water, ice, and frost through their distinct dielectric properties[54], providing high sensitivity and rapid response times[55, 56]. The ability to print or deposit these sensors directly onto surfaces enables accurate detection of frost or ice coverage across the monitored area[57]. Besides, capacitive sensors operate with low power consumption and can be easily integrated into existing defrosting systems[58]. The ability to differentiate vapor, liquid and solid phases through direct sensing without the complexity of optical methods, makes capacitive sensing an ideal

Supplementary Information, including one PDF document and seven video files, is available.

complement to SAW-based defrosting/deicing systems, enabling on-demand energy-efficient frost and ice removal.

In this study, we propose a synergistic approach that integrates nanovibration with QLS, complemented by a capacitive sensing mechanism. Our method leverages the unique properties of QLS for reduced adhesion in combination with surface nanovibration for rapid removal of condensate, frost, and ice while utilizing capacitive sensing to enable targeted detection and efficient removal. Unlike existing methods, our approach minimizes energy consumption while providing a versatile solution applicable across multiple fields, such as refrigeration, air conditioning and transportation systems. The synergistic combination of surface engineering, surface nanovibration, and intelligent sensing represents a transformative approach to addressing the longstanding challenges of condensate, frost, and ice accretions.

Results & discussion

Design of the sensor-assisted nanovibrational QLS

A synergistic sensing-actuation slippery surface was designed for condensate, frost and ice detection, prevention and removal as shown in Fig. 1a (fabrication details in *Methods* and Supplementary Fig. S1). This design comprised two components: an integrated QLS and SAW actuator for removal and a capacitive sensing component for detection on one piece. The side view reveals the layered structure consisting of a QLS coating (surface treatment in *Methods* and Supplementary Fig. S2) chemically bonded to the SiO_2 passivation layer (50 nm), which covers the patterns of acoustic interdigital transducer (IDT) and sensor electrodes. The acoustic waves propagate across the surface as indicated by the wave arrow to interact with each condensed droplet at the interface. The dual-functional configuration of the device ensures effective droplet removal while maintaining reliable detection capability, which significantly improves energy efficiency by enabling on-demand removal only when droplets are detected. QLS as the top interface provides durable slipperiness[59] (surface characterization in *Methods* and Supplementary Fig. S3-S4) to reduce droplet retention force and facilitate efficient removal under SAW actuation.

Supplementary Information, including one PDF document and seven video files, is available.

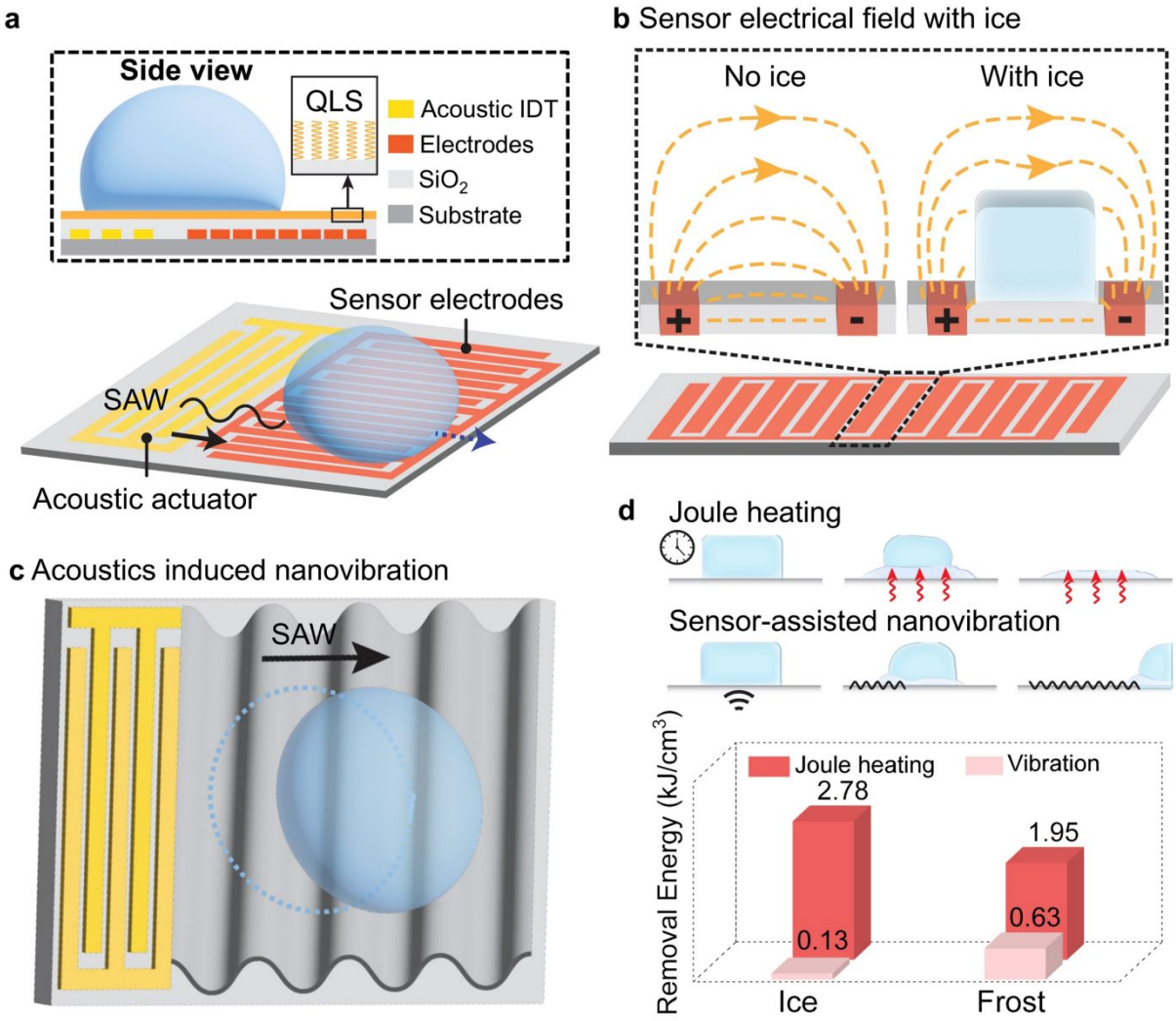

Fig. 1: Design of sensor-assisted vibrational QLS. a, Diagram of a synergistic droplet removal system with an acoustic actuator and a capacitive sensor on a QLS surface. **b**, Schematic illustration of the capacitive sensor induced electrical field under the influence of the ice. **c**, Droplet removal by nanovibration. **d**, Top: Diagrams of the deicing using Joule heating and the sensor-assisted nanovibration; Bottom: the energy consumption of ice and frost removal using these two methods.

This sensing-actuation design incorporates two functions. The first is the capacitive sensing component (Fig. 1b; Supplementary Fig. S5) which utilizes interdigitated electrodes to generate an electrical field that enables precise detection of different phase states on the surface. The presence of ice significantly alters the electrical field distribution between the electrodes due to its distinct dielectric properties compared with air (Fig. 1b, Supplementary Table 1). The electrode configuration was optimized through simulations to achieve maximum sensitivity and detection

Supplementary Information, including one PDF document and seven video files, is available.

accuracy (Supplementary Fig. S6), while maintaining excellent stability under different humidity conditions (Supplementary Fig. S7). The second is the removal mechanism of surface nanovibration, where SAWs are generated by the IDT and propagate across the surface (Fig 1c.). When acoustic waves encounter a liquid droplet, they induce localized nanovibration at the solid-liquid interface. The SAW device was specially designed with 300 μm wavelength and 13.36 MHz working frequency to maximize the acoustic energy transfer into the droplet[45] (Supplementary Fig. S8). A comparative study with a lower-frequency device (6.53 MHz) confirmed that 13.36 MHz offers better removal performance at the same power input (Supplementary Fig. S9, Supplementary Video 1). The actuation amplitude was also optimized for effective removal (Supplementary Fig. S10). These interactions result in efficient droplet removal from the slippery surface. In fact, this system is capable of detecting and removing droplets, frost, and ice. Compared to conventional Joule heating methods which operate on fixed time intervals[40], the sensor-assisted nanovibrational surface enables on-demand removal, significantly improving energy efficiency, resulting in 68% and 95% energy savings for frost and ice removal, respectively (Fig. 1d, see Supplementary Note 1 for energy consumption analysis). This direct removal using nanovibration focuses on physically displacing condensate and ice rather than relying on Joule heating and thus does not consume energy for the complete melting of ice and the evaporation of liquid droplets.

Frost removal via surface nanovibration

We demonstrated the effectiveness of nanovibrational removal for both condensate and frost as condensate removal plays a crucial role in frosting mitigation. Condensation-frosting experiments were performed on a cold plate with real-time heat flux measurements to examine the adverse effects of condensate and frost on heat transfer (measurement details in *Method* and Supplementary Fig. S11). The frost formation process begins with water vapor condensing into droplets on the subcooled surface, which subsequently transforms into a dense frost layer through freezing and crystal growth (Fig. 2a). After defrosting, the frost melts into liquid droplets that can be effectively removed from the surface. The temporal evolution of surface temperature and heat flux during this process is captured in Fig. 2b. As the surface temperature gradually decreases, the heat flux exhibits a characteristic peak when frosting initiates (marked by the blue shaded region), indicating the onset of frost formation. Following this peak, the heat flux shows a continuous decline as the

Supplementary Information, including one PDF document and seven video files, is available.

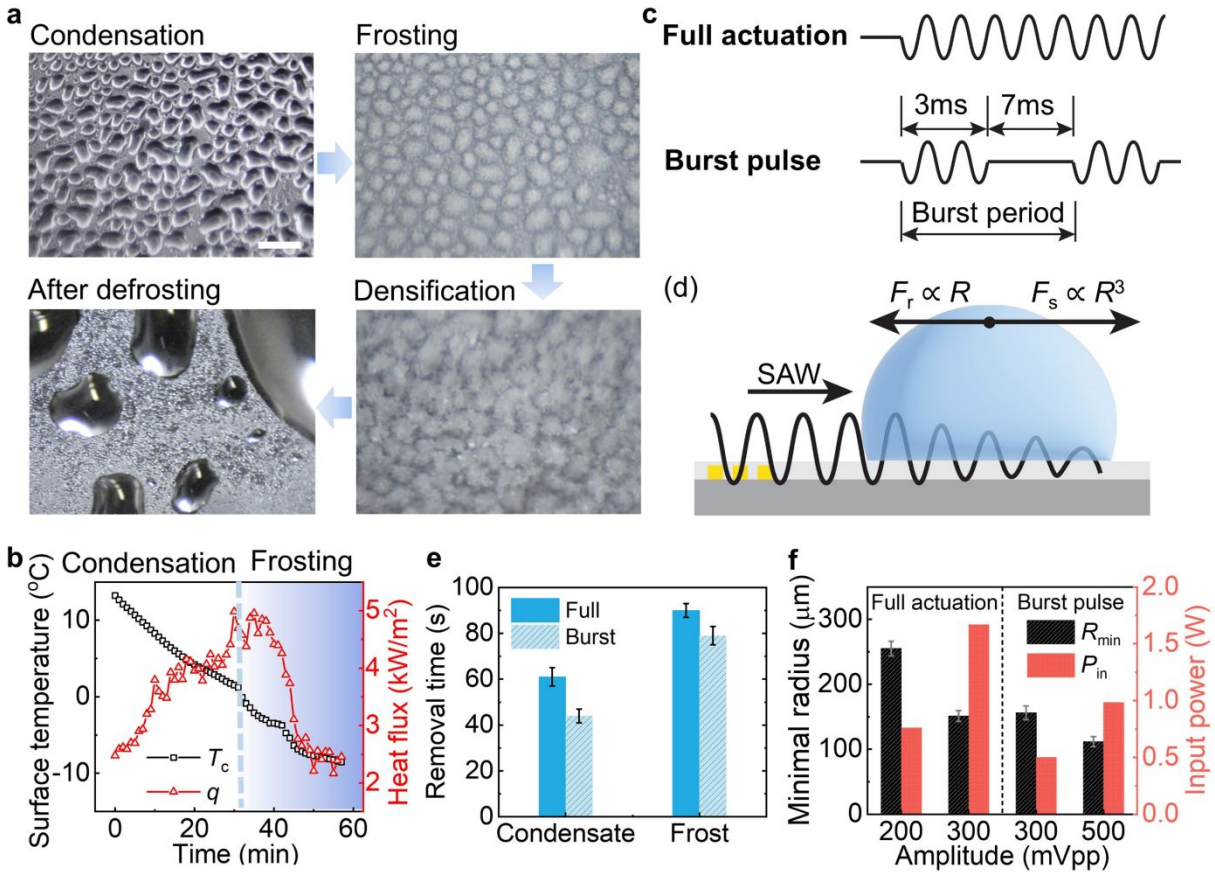

Fig. 2: Frost removal by surface vibration. a, Images of condensation frosting and defrosting on a cold plate, scale bar: 1 mm. **b**, Surface temperature and heat flux changes during the condensation frosting on a cooling surface, blue color area stands for frosting starts. **c**, Different modes of acoustic actuation. **d**, Schematic diagram of the droplet force balance under SAW on a horizontal surface. **e**, Comparison of the removal time using SAW at full and burst mode for condensate and frost removal. **f**, Minimum droplet size that can be removed at continuous/pulse modes with different amplitudes and the corresponding input power to the acoustic IDT.

frost layer accumulates, acting as a growing thermal barrier that increasingly impedes heat transfer between the cold surface and the ambient environment. This progression from condensation to frosting reduces the heat transfer rate and decreases the energy efficiency of thermal systems. Effective removal of condensates, frost and ice is therefore crucial for maintaining system performance.

Therefore, we deposited an acoustic IDT onto a substrate and mounted it on a Peltier cooling stage to systematically investigate their capability for condensate and frost removal under controlled temperature conditions (experimental setups in *Methods* and Supplementary Fig. S12). To achieve efficient removal, two acoustic actuation modes were implemented: full actuation and

Supplementary Information, including one PDF document and seven video files, is available.

burst pulse (Fig. 2c). The full actuation mode provided continuous nanovibration, while burst mode operated with an actuation ratio of 30%, actuating for 3 ms followed by 7 ms rest. The actuation ratio represents the percentage of time the acoustic IDT is actively vibrating within each burst period. When the acoustic waves interact with a droplet, the droplet experiences two competing forces: a retention force (F_r) arising from the surface-liquid contact that scales linearly with the droplet radius[60] (i.e. $F_r \propto R$), and a streaming force (F_s) generated by SAW actuation that scales with the cube of the radius (i.e. $F_s \propto R^3$) (Fig. 2d). The droplet movement is determined by the balance between these competing forces (see Supplementary Note 2 for detailed force analysis). Under the same average input power, our experimental results show that both modes can effectively remove condensate and frost (Fig. 2e). Notably, the burst mode achieves comparable shorter removal times as it allows higher nanovibration amplitude during the active periods due to the intermittent nature of power input. This higher amplitude capability of burst mode increases the vibration amplitude and enables the removal of smaller droplets. The results show that burst mode maintains effective removal with lower overall average power input compared to continuous actuation (Fig. 2f). The power efficiency of burst mode becomes particularly evident when comparing the two modes at the same amplitude. For instance, when 300 mVpp amplitude was applied for both full and burst modes, the burst mode achieved similar minimum removable droplet sizes while consuming approximately 3 times less power than full actuation (Fig. 2f). These findings demonstrate that burst mode not only saves energy but also enhances removal performance through higher instantaneous nanovibration amplitudes.

Quasi-liquid surface reduces retention force for effective removal

To achieve efficient acoustic removal of condensate and frost, especially on horizontal surfaces, surface engineering plays a crucial role in reducing retention forces. The significance of surface properties is clearly demonstrated through comparative experiments between hydrophilic surface and QLS under nanovibration (Fig. 3a, b). On a hydrophilic surface, nanovibration causes droplets to coalesce and form a continuous water film that remains pinned to the surface even after prolonged acoustic actuation (Fig. 3a, left). In contrast, QLS significantly reduces the retention force between the liquid and the substrate, enabling rapid droplet removal within 0.04s after

Supplementary Information, including one PDF document and seven video files, is available.

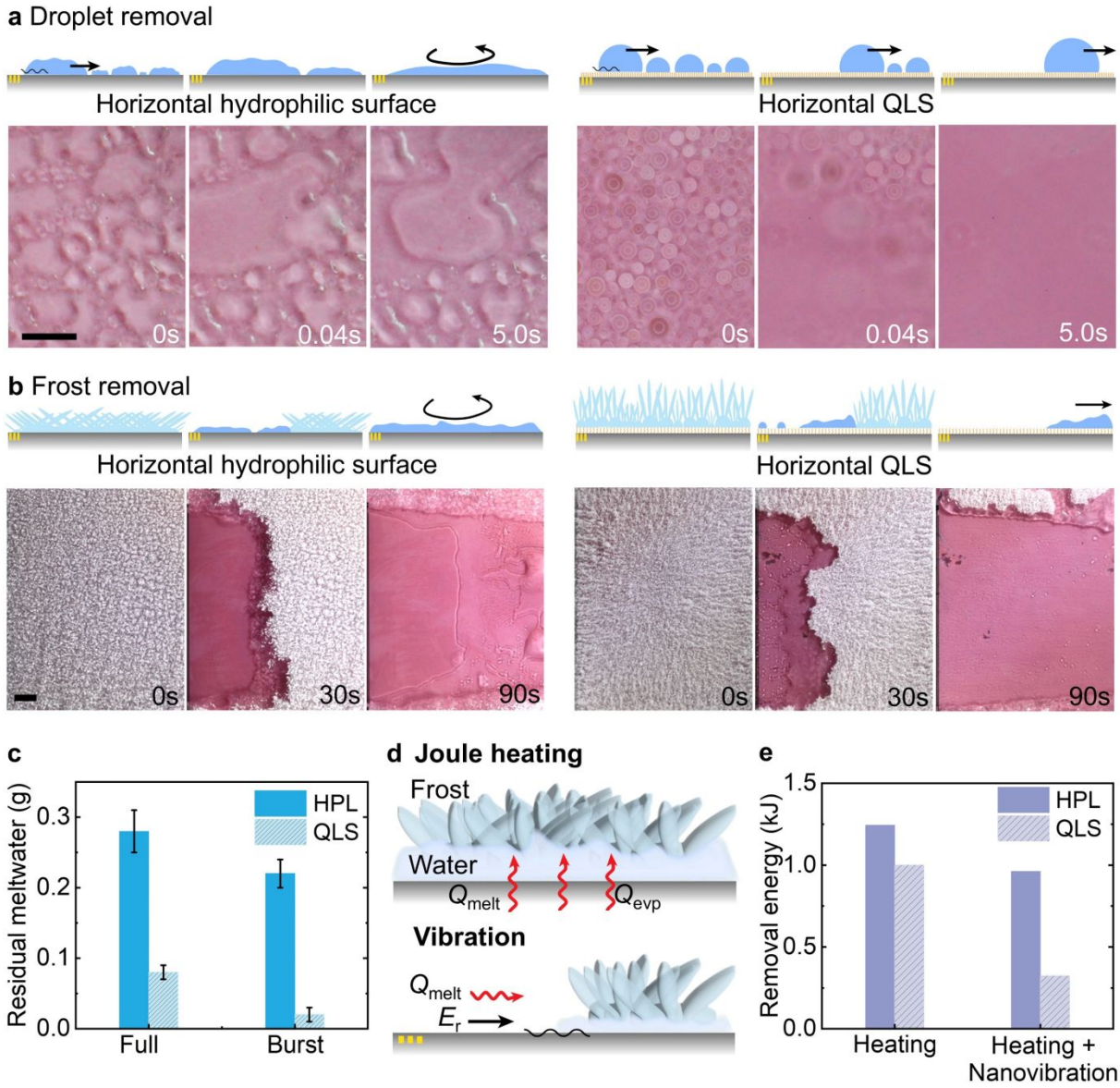

Fig. 3: The role of QLS in condensate and frost removal. a, Images of droplet removal using SAW on hydrophilic and QLS surfaces. SAW direction is from left to right. Scale bar: 0.5 mm. **b**, Images of frost removal using SAW on hydrophilic and QLS surfaces, scale bar: 2 mm. **c**, Comparison of the residues after frost removal on hydrophilic (HPL) and QLS surfaces at full/burst mode. **d**, Schematics of different energy sources used for Joule heat (upper) and SAW (bottom) in frost removal. Here, Q_{melt} is the heat melts the frost, Q_{evp} is the heat vaporizes the remaining water, and E_r is the acoustic removal energy. **e**, Comparison of the energy consumption for frost removal using Joule heating and combination of SAW and heating on HPL and QLS surfaces.

turning on the nanovibration (Fig. 3a, right). The SAW-induced streaming force efficiently propels droplets that reach the critical removal size, causing them to sweep across the surface and merge

Supplementary Information, including one PDF document and seven video files, is available.

with neighboring droplets (Supplementary Video 2). This cascading removal process results in a clean surface within 5 s, demonstrating the significant role of QLS in reducing retention force for droplet removal (Supplementary Video 3). We observed similar behaviors during frost removal (Fig. 3b). When SAW is applied, frost melts on both surfaces, but their removal mechanisms differ significantly. On the hydrophilic surface, the melted frost transforms into a persistent water film that remains pinned despite continued acoustic actuation. While on the QLS, the melting process is accompanied by simultaneous water removal - as the melting front proceeds, the resulting water is continuously removed by SAW forces. Additionally, the hydrophobic nature of QLS promotes the formation of discrete droplets rather than a continuous film, allowing these droplets to be efficiently removed by surface nanovibration (Supplementary Video 4). This synergistic effect results in complete frost removal within 90 s, leaving a clean surface (Supplementary Video 5).

We quantified the enhanced frost removal on QLS by measuring residual meltwater after removal using both full and burst mode actuations (Fig. 3c). The QLS consistently shows a lower residual mass (71% less in full mode and 86% less in burst mode) compared to the hydrophilic surface (HPL), with burst mode achieving even higher removal efficiency while maintaining lower energy consumption (Supplementary Note 3). To understand the energy dynamics during frost removal, we examined two primary removal mechanisms: Joule heating and surface nanovibration (Fig. 3d, see Supplementary Note 1 for detailed energy analysis). In Joule heating, energy is primarily consumed for melting (Q_{melt}) and evaporation (Q_{evp}), while nanovibration combines efficient melting with mechanical removal (E_r). The energy consumption comparison (Fig. 3e) reveals that surface nanovibration requires significantly less energy compared to heating methods, particularly saving 75% energy when applied to the QLS. This demonstrates that nanovibration-induced mechanical removal can save tremendous energy without complete water evaporation. The synergistic integration of surface nanovibration with QLS thus offers a promising pathway for achieving dramatically improved energy efficiency in frost control applications.

Capacitive sensing mechanism and frost detection performance

The planar interdigital capacitive sensor design demonstrates robust detection capabilities across different stages of the frost formation process (Fig. 4a). The simulated electric field distributions show distinctive responses with and without water (Supplementary Fig. S6), highlighting the

Supplementary Information, including one PDF document and seven video files, is available.

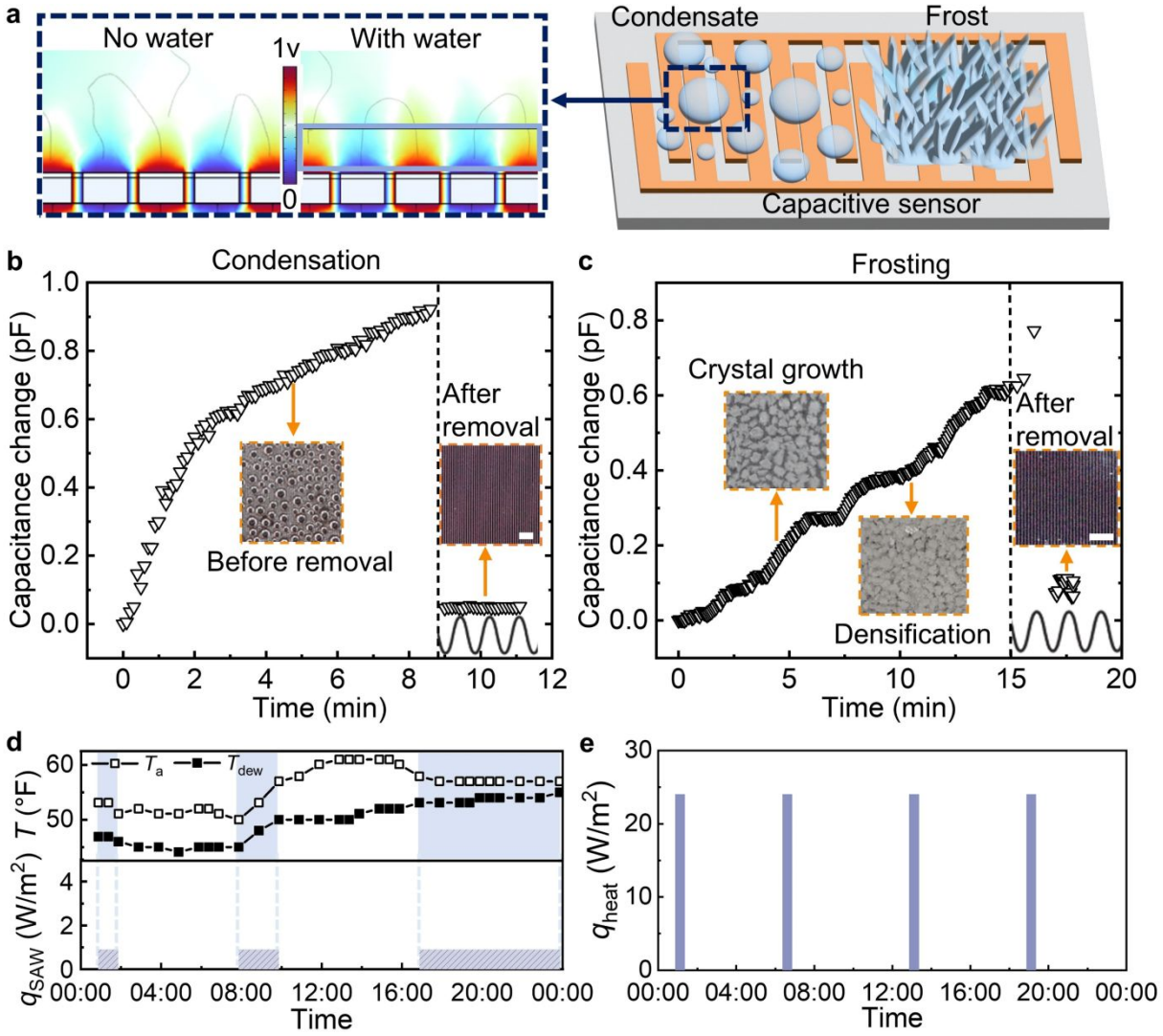

Fig. 4: Capacitive sensing-assisted frost detection and removal. a, An interdigital capacitive sensor was used for detection of condensate, frost and ice. Electrical field was affected by the condensate which provides a capacitance signal, result from simulation. Capacitance signal changed during the **b,** Condensation and **c**, frosting, followed by removal using SAW, scale bar: 0.5 mm. **d**, Air and dew point temperature variation (T_a and T_{dew}) during 12/25/2023 at Rock Hill, SC. **e**, Daily energy consumption comparison of the condensation removal using synergic sensor and SAW method and traditional time-based defrosting.

capability to detect the presence of condensate (Fig. 4a top). The sensor can detect both condensate droplets and frost formations, corresponding to the two primary stages of condensation frosting (Fig. 4a bottom, see Supplementary Fig. S13 for detailed sensor calibration).

Supplementary Information, including one PDF document and seven video files, is available.

The temporal evolution of capacitance during condensation and frost formation reveals distinct patterns characteristic of different frosting stages. The capacitance (ΔC) exhibits a rapid initial increase followed by gradual saturation during condensation (Fig. 4b). This non-linear response can be attributed to the enhanced sensitivity of the sensor to the change of initial surface coverage, where small droplets coalesce and spread across the electrode array. The subsequent plateauing reflects the reduced marginal impact of further condensation on the wetted surface. Upon the activation of nanovibration, the capacitance returns to baseline levels, indicating effective droplet removal. The frosting process presents a more complex capacitive response characterized by a multi-stage evolution (Fig. 4c). The initial gradual increase corresponds to crystal nucleation and growth, followed by notable fluctuations during the densification phase. These oscillations reflect the dynamic nature of frost layer development, where concurrent processes of crystal growth, melting, and restructuring occur due to local heat and mass transfer phenomena[48]. When nanovibrational removal is activated, a characteristic spike in capacitance is observed (Fig. 4c after 15 min), corresponding to the temporary formation of liquid water during melting due to the higher dielectric constant of water, followed by rapid removal and return to near-baseline conditions.

To demonstrate the practical advantages of this sensor-integrated approach, we analyzed meteorological data (source: weatherspark.com) from Rock Hill in South Carolina in winter (Fig. 4d). The relationship between ambient temperature (T_a) and dew point temperature (T_{dew}) indicates potential frosting periods when the heat pump evaporator surface temperature falls below the dew point temperature (blue rectangular area in Fig. 4d top). In fact, the heat pump temperature is typically 5-15℃ below ambient temperature, enabling the formation of condensate and frost in winter[61]. By utilizing capacitive sensing, defrosting operations can be precisely triggered based on actual frost formation rather than fixed time intervals. The energy efficiency analysis of this sensor-assisted approach is quantified in Fig. 4e, comparing our method with conventional time-based defrosting protocols (operating on 6-hour cycles with 30-minute defrost periods). The capacitive sensor enables targeted, on-demand frost removal, resulting in substantial energy savings by eliminating unnecessary defrost cycles during frost-free periods. Our sensor-assisted nanovibrational surface consumes 3.8 times less energy than traditional defrosting methods that rely on 30-minute Joule heating cycles every 6 hours (see Supplementary Note 1 for detailed energy consumption analysis). This integration of precise capacitive sensing with nanovibrational

Supplementary Information, including one PDF document and seven video files, is available.

surface represents a significant advancement in frost management, enabling real-time monitoring and energy-efficient operation for cold-climate heat pumps.

Ice detection and removal via surface nanovibration

Following the demonstrated frost management capabilities, the integrated sensing-actuation system exhibits effective performance in ice detection and removal (Fig. 5a, b, and c). As illustrated in Fig. 5a, the device achieves complete ice removal on QLS, whereas conventional hydrophilic surfaces retain residual water films despite identical nanovibrations. The hydrophilic surface exhibits a characteristic rotational movement of the melted ice layer under surface nanovibrations, while it fails to achieve removal due to strong surface adhesion (Supplementary Movie 5). On the QLS, the melted ice layer experiences reduced adhesion forces and responds to SAW-induced streaming forces by directional movement, leading to complete removal within 100 s. Notably, the ice removal mechanism operates through interfacial melting at the ice-substrate interface, where the interfacial water layer aids the removal of the bulk ice before complete melting. This distinct behavior arises from the combined effects of thermo-mechanical interaction of the SAW at the solid-liquid interface when the streaming-dominated driving force overcomes the surface retention force to the ice. Unlike frost removal which requires complete melting before displacement, ice removal relies on SAW energy concentrating at the ice-substrate interface, causing interfacial melting between ice and the substrate. The formation of a thin water layer reduces ice-substrate adhesion, while acoustic streaming provides sufficient driving forces to move the entire ice structure as a single unit. This contrast in removal mechanisms can be further attributed to their difference in surface continuity: frost, being composed of loosely connected microcrystals, allows for progressive melting and flow, while ice forms a continuous solid phase that moves as a whole (Supplementary Note 4, Supplementary Video 6).

Performance analysis under different actuation modes demonstrates robust ice removal capabilities, with a ‘full-burst’ mode which began with 20 seconds of full actuation followed by burst mode operation. As shown in Fig. 5d, both full and full-burst modes achieve effective melting and removal on QLS, with full-burst mode offering lower energy consumption. In full-burst mode, initial full actuation melts ice at the ice-substrate interface, followed by high-amplitude burst actuation to push away the ice with enhanced driving force (Supplementary Note 3). The measurements of residual liquids confirm complete ice removal on QLS. To evaluate its durability

Supplementary Information, including one PDF document and seven video files, is available.

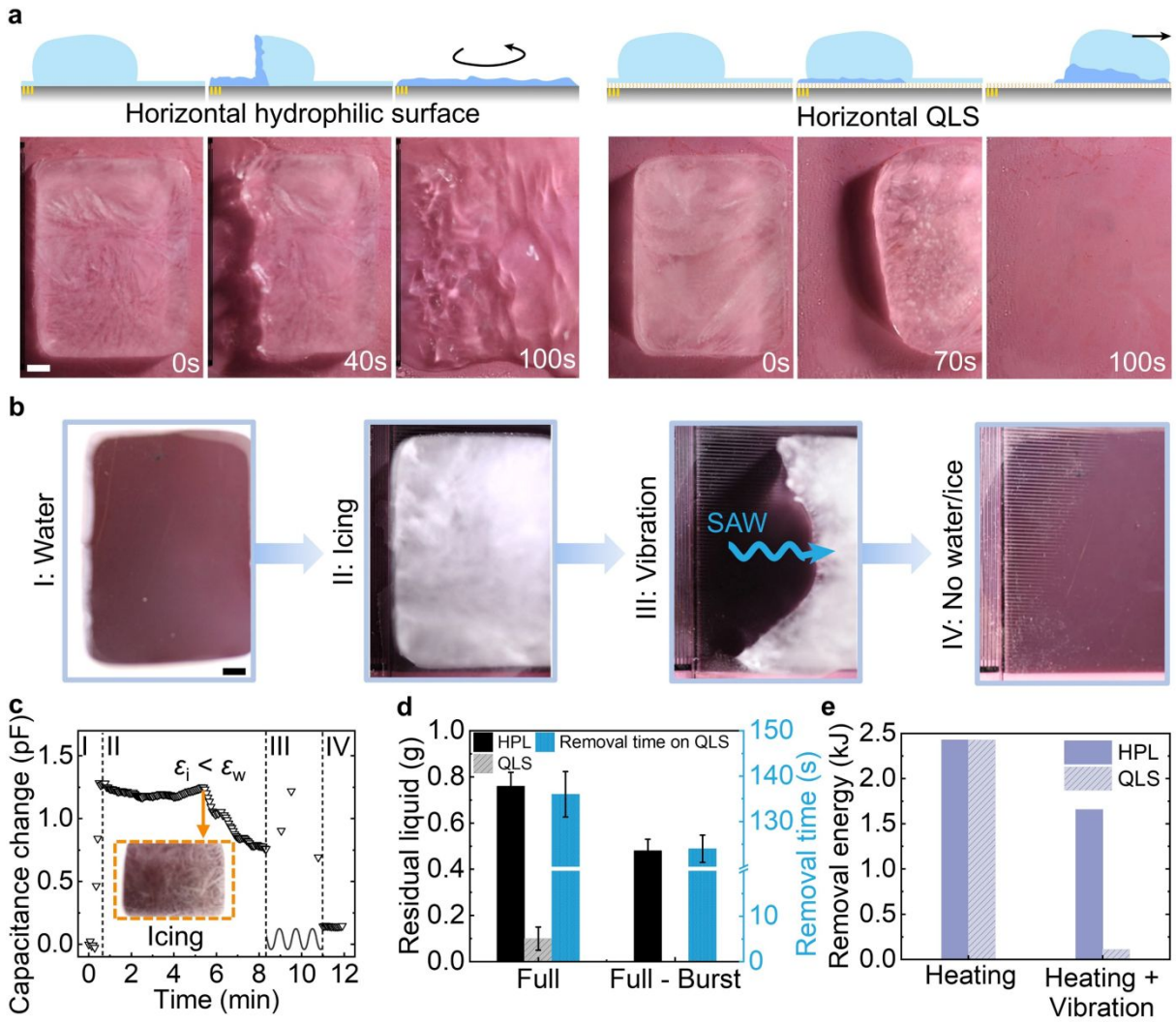

Fig. 5: Ice detection and removal via surface vibration. a, Schematic diagrams and images of ice removal mechanism on hydrophilic surface (left) and QLS (right), scale bar: 2 mm. **b**, Images of each stage during icing and ice removal on QLS, scale bar: 2 mm. **c**, capacitance change during the icing and removal by surface vibration. **d**, Comparison of the residues after ice removal and the removal time on hydrophilic surface and QLS with SAW at full/burst mode. No residual liquid for full-burst mode on QLS. **e**, Comparison of the ice removal energy consumption using Joule heating and combined Joule heating with surface vibration.

and long-term performance, we conducted 100 icing/deicing cycles, during which the device consistently maintained fast and complete removal without degradation in function or efficiency (Supplementary Fig. S14, Supplementary Video 7). Energy efficiency analysis demonstrates that the integrated approach consumes 95% less energy compared to traditional Joule heating (Fig. 5e). By combining on-demand SAW actuation with minimal heating, our approach achieves complete ice removal while substantially reducing energy requirements (Supplementary Note 1). This

Supplementary Information, including one PDF document and seven video files, is available.

successful demonstration of ice removal and detection capabilities, alongside previously demonstrated frost management, establishes the synergistic approach as a versatile solution for frost and ice control.

The complete ice formation and removal process on QLS comprises four characteristic stages: *I* initial water presence, *II* complete ice formation, *III* SAW-induced removal through combined melting and nanovibration, and *IV* cleared surface state (Fig. 5b). The capacitive sensing system effectively tracked these phase transitions in real-time (Fig. 5c). The capacitance provides distinct indications for each stage: water deposition produces an initial elevated signal due to high dielectric constant of water, followed by a marked decrease during ice formation as the dielectric constant of ice is smaller than water (Supplementary Table 1), and finally a characteristic peak-and-drop pattern during the removal as ice partially melts before leaving from the surface.

Discussion

In summary, our study has demonstrated high-efficiency frost and ice control via sensing-assisted nanovibrational slippery surfaces. The surface acoustic waves induced nanovibration provides efficient mechanical removal without complete melting or evaporation. Moreover, the quasi-liquid surface reduces the retention forces while capacitive sensing offers precise phase detection to minimize energy waste. By synergistically integrating these three components, we have addressed the fundamental limitations of conventional energy-intensive thermal approaches for defrosting and deicing. By activating the on-demand nanovibrational surface in precise timeframes, we are able to save 68% and 95% energy for frost and ice removal, respectively. The real-time detection capabilities enable on-demand energy consumption for activation, eliminating unnecessary defrosting and deicing cycles and resulting in 3.8 times lower energy consumption compared to traditional time-based protocols that rely on 30-minute Joule heating cycles every 6 hours. For future large-scale applications, low-cost piezoceramic actuators, simplified sensor fabrication, and localized sensing strategies can enhance scalability. Batch processing and modular designs offer further opportunities to reduce manufacturing costs. These improvements, together with the demonstrated energy efficiency, establish a promising strategy for broad integration in systems such as heat pumps, refrigeration units, and transportation systems.

Supplementary Information, including one PDF document and seven video files, is available.

Experimental

Fabrication of the sensor-assisted nanovibrational QLS

The acoustic interdigital transducer and capacitive sensor electrodes were simultaneously fabricated on a $LiNbO_3$ piezoelectric substrate (4 inches, 128° Y-cut, University Wafer) through standard lithography and subsequent metal deposition process (Fig. S1). Initially, all wafers were rinsed with acetone and DI water. After drying using pure nitrogen gas, the substrates were treated with hexamethyldisilane (HMDS) for 20 min to promote the adhesion of the photoresist. A negative photoresist (NLOF2020) was then spin-coated onto the substrate with 1-min soft baking at 115 °C. The coated substrate was exposed under the i-line in an ultraviolet printer (Karl Suss Contact Printer MABA6 Gen4) and the pattern was developed in AZ300 MIF, followed by a post-development bake at 115°C for 1 min. The substrate was then cleaned using a low-power O_2 plasma (50 W, 200 mT) for 20 s to remove undeveloped photoresist before depositing a tri-layer metallization stack of Cr-Au-Cr (50 nm-300 nm-10 nm). Lift-off was performed by immersing the samples in AZ400T stripper at 80°C for 3 hours, followed by thorough DI water spray cleaning to remove residual photoresist. The contact pads of the electrodes of both IDTs and capacitive electrodes were covered and a 50 nm SiO_2 passivation layer was deposited to prevent short circuits during aqueous operation.

QLS was then coated on the fabricated device through a liquid-phase grafting process (Fig. S2). Initially, the surface was cleaned with O_2 plasma to generate hydroxyl groups for subsequent modification. The QLS treatment was performed using a one-step grafting method, where the silicone oil (viscosity: 500 cSt, Gelest Inc.) was drop-casted on the device and heated at 150°C for 1 h to chemically tether flexible polymer chains to the surface. To remove excess unbonded silicone oil, the siloxane-grafted substrates were subsequently cleaned in a toluene bath with mechanical agitation for 2 min, resulting in a clean QLS coating. Atomic force microscopy (AFM) measurements for QLS surfaces were carried out before and after defrosting/deicing (Fig. S4).

Surface characterization

Surface characterization was performed to evaluate the wetting properties of the fabricated surfaces. As illustrated in Fig. S3a, QLS consists of a flexible polymer layer grafted onto the

Supplementary Information, including one PDF document and seven video files, is available.

substrate, which makes it hydrophobic and slippery to droplets. The chemical structure formula of QLS is shown in Fig. S3b, where polydimethylsiloxane chains are covalently bonded to the substrate through O-Si-O linkages, creating a uniform molecular brush structure. Surface wettability measurements were conducted using a goniometer (Model 290, ramé-hart) under ambient conditions (20-22°C, ~50% relative humidity). Static contact angles and contact angle hysteresis (CAH) were measured by depositing 5 μL water droplets, with values averaged from 5 independent measurements. As shown in Fig. S3c, QLS demonstrated superior water-repellent properties with a high static contact angle of 108° ± 3° and minimal CAH of 1.5° ± 0.2°, whereas the hydrophilic surface (HPL) exhibited a low contact angle of 5.8° with significantly higher CAH of 20°. The contact angle hysteresis was determined by tilting the surface from horizontal until droplet motion was initiated, at which point the advancing and receding angles were measured using software support (Ramé-hart).

Condensation frosting surface heat flux measurement and thermal resistance network analysis

The heat flux through an aluminum block (5 cm × 5 cm) during the condensation frosting was measured using a temperature gradient method. As shown in Fig S11a, the block was thermally coupled to a cold plate maintained at -10°C by a chiller (FL1201, Julabo). Two K-type thermocouples (Omega Engineering) were embedded in the aluminum block at a vertical separation distance L, measuring the temperatures at the top (T_t) and bottom (T_b) positions. The temperatures were recorded by a data logger (DAQ970A, Keysight) and processed in LabVIEW. The local heat flux was calculated using Fourier's law of conduction: $q = -k_{al}(T_t - T_b)/L$, where k_{al} is the thermal conductivity of aluminum. The thermal resistance network diagrams illustrate the heat transfer mechanism before and after frost removal (Fig. S11b). Before defrosting, the presence of frost introduces an additional thermal resistance (R_i) in series with the plate resistance (R_p), which impedes heat transfer between the liquid side (T_l) and air (T_a). After frost removal, this additional thermal resistance is eliminated, leaving only the plate resistance R_p in the thermal pathway. Consequently, the removal of the frost layer significantly reduces the total thermal resistance, resulting in enhanced heat flux through the system.

Supplementary Information, including one PDF document and seven video files, is available.

Experimental Setup for Capacitive Sensing and Acoustic Removal

The condensation, icing, frosting and subsequential SAW removal experiment was performed using a temperature-controlled setup coupled with electrical measurements (Fig S12). The device was mounted on a Peltier stage (CP-200TT, TE Technology) that provided precise surface temperature control for different testing conditions: 5°C for condensation studies and -10°C for frost/ice formation experiments. The experiment was carried out at room temperature (20-22°C), with the water vapor supply from a humidifier (RH > 90%). The SAW removal process started after 1 min for condensation, 15 min for frosting, and 5 min for complete icing. The acoustic IDTs were driven by a function generator (33500B, Keysight) connected to an RF amplifier (2100L, Electronics and Innovation Ltd.) to generate SAW upon the device. The electrical performance was monitored using an oscilloscope (DHO800, Rigol Technologies) and a current probe (TCP312A, Tektronix) for voltage and current passing through the device for power measurement. For sensing experiments, the capacitive sensor started the signal recording (SNOC028, Sensing Solutions EVM GUI Tool, Texas Instruments) immediately after the sample was put on the stage, and turned off during the removal process due to electrical interference.

Data availability

The data that supports the plots within this paper and other findings of this study are available from the corresponding authors upon reasonable request.

References

1. M. R. Nasr, M. Fauchoux, R. W. Besant and C. J. Simonson, *Renew. Sust. Energ. Rev.*, 2014, **30**, 538-554.
2. S. Nath, S. F. Ahmadi and J. B. Boreyko, *Nanoscale Microscale Thermophys. Eng.* , 2017, **21**, 81-101.
3. S. Mestres, H. Pons-Rejraji, B. Pereira, C. Bouche, A. Vega, L. Chaput, S. Vorilhon, L. Janny and F. Brugnon, *Cryobiology*, 2020, **94**, 32-39.
4. M. H. Nazir, Z. A. Khan, A. Saeed and K. Stokes, *Eng. Fail. Anal.* , 2016, **63**, 43-60.
5. M. Farzaneh, *Atmospheric icing of power networks*, Springer Science & Business Media, 2008.
6. Y. H. Cao, W. Y. Tan and Z. L. Wu, *Aerosp. Sci. Technol.* , 2018, **75**, 353-385.

Supplementary Information, including one PDF document and seven video files, is available.

7. C. Y. Khor, M. Z. Abdullah, H. J. T. Tan, W. C. Leong and D. Ramdan, *Microelectron. Reliab.* , 2012, **52**, 241-252.
8. M. S. Patil, J.-H. Seo and M.-Y. Lee, *Appl. Therm. Eng.*, 2017, **113**, 1071-1087.
9. J. Lv, Y. Song, L. Jiang and J. Wang, *ACS Nano*, 2014, **8**, 3152-3169.
10. L. Guo, L. Zhou, M. Chen and W. Huang, *IET Generation, Transmission Distribution*, 2016, **10**, 1969-1975.
11. C. Ryerson, T. Gilligan and G. Koenig, 1999.
12. J. B. Boreyko, R. R. Hansen, K. R. Murphy, S. Nath, S. T. Retterer and C. P. Collier, *Sci. Rep.*, 2016, **6**, 19131.
13. Y. Yao, T. Y. Zhao, C. Machado, E. Feldman, N. A. Patankar and K.-C. Park, *Proc. Natl. Acad. Sci. U. S. A.*, 2020, **117**, 6323-6329.
14. N. Miljkovic, R. Enright, Y. Nam, K. Lopez, N. Dou, J. Sack and E. N. Wang, *Nano Lett.*, 2013, **13**, 179-187.
15. D. Wang, Q. Sun, M. J. Hokkanen, C. Zhang, F. Y. Lin, Q. Liu, S. P. Zhu, T. Zhou, Q. Chang, B. He, Q. Zhou, L. Chen, Z. Wang, R. H. A. Ras and X. Deng, *Nature*, 2020, **582**, 55-59.
16. J. B. Boreyko and C.-H. Chen, *Phys. Rev. Lett.*, 2009, **103**, 184501.
17. T. Verho, C. Bower, P. Andrew, S. Franssila, O. Ikkala and R. H. Ras, *Adv. Mater.*, 2011, **23**, 673-678.
18. T. S. Wong, S. H. Kang, S. K. Tang, E. J. Smythe, B. D. Hatton, A. Grinthal and J. Aizenberg, *Nature*, 2011, **477**, 443-447.
19. P. Kim, T. S. Wong, J. Alvarenga, M. J. Kreder, W. E. Adorno-Martinez and J. Aizenberg, *ACS Nano*, 2012, **6**, 6569-6577.
20. A. K. Epstein, T. S. Wong, R. A. Belisle, E. M. Boggs and J. Aizenberg, *Proc. Natl. Acad. Sci. U.S.A.*, 2012, **109**, 13182-13187.
21. J. S. Wexler, I. Jacobi and H. A. Stone, *Phys. Rev. Lett.*, 2015, **114**, 168301.
22. M. Villegas, Y. Zhang, N. Abu Jarad, L. Soleymani and T. F. Didar, *ACS Nano*, 2019, **13**, 8517-8536.
23. J. Sarma, L. Zhang, Z. Q. Guo and X. M. Dai, *Chem. Eng. J.*, 2022, **431**, 133475.
24. L. Zhang, Z. Guo, J. Sarma and X. Dai, *ACS Appl. Mater. Interfaces*, 2020, **12**, 20084-20095.
25. Z. Azimi Dijvejin, M. C. Jain, R. Kozak, M. H. Zarifi and K. Golovin, *Nat. Commun.*, 2022, **13**, 5119.
26. K. Golovin, A. Dhyani, M. Thouless and A. Tuteja, *Science*, 2019, **364**, 371-375.
27. P. Irajizad, A. Al-Bayati, B. Eslami, T. Shafquat, M. Nazari, P. Jafari, V. Kashyap, A. Masoudi, D. Araya and H. Ghasemi, *Mater. Horiz.*, 2019, **6**, 758-766.
28. S. Chavan, T. Foulkes, Y. Gurumukhi, K. Boyina, K. F. Rabbi and N. Miljkovic, *Appl. Phys. Lett.*, 2019, **115**.
29. D. Wang, J. D. Jiang, L. R. Tao, Z. L. Kou and L. F. Yao, *Appl. Therm. Eng.*, 2017, **127**, 1267-1273.
30. R. J. Zhao, Z. P. Wang, D. Huang, W. H. Shen, H. H. Hu and X. Q. Tang, *Appl. Therm. Eng.*, 2023, **226**, 120147.
31. D. Huang, Q. X. Li and M. L. Yuan, *Appl. Energy* 2009, **86**, 1697-1703.
32. H. J. Choi, B. S. Kim, D. Kang and K. C. Kim, *Appl. Energy* 2011, **88**, 4544-4555.
33. K. Nawaz, A. F. Elatar and B. A. Fricke, 2018.
34. T. Xie, J. K. Dong, H. W. Chen, Y. Q. Jiang and Y. Yao, *Energy*, 2016, **116**, 998-1005.

Supplementary Information, including one PDF document and seven video files, is available.

35. P. Guo, Z. Y. Teng, X. Han, Y. Sun, R. Y. Jin, L. Jiang and L. P. Heng, *Chem. Eng. J.*, 2023, **471**, 144518.
36. H. Q. Zhang, G. L. Zhao, S. W. Wu, Y. Alsaid, W. Z. Zhao, X. Yan, L. Liu, G. S. Zou, J. Y. Lv, X. M. He, Z. Y. He and J. J. Wang, *Proc. Natl. Acad. Sci. U. S. A.*, 2021, **118**, e2100978118.
37. H. H. Tan, G. H. Xu, T. F. Tao, S. C. Zhang and A. L. Luo, *Appl. Therm. Eng.*, 2016, **107**, 479-492.
38. Z. Goraj, 2004.
39. G. Heydari, E. Tyrode, C. Visnevskij, R. Makuska and P. M. Claesson, *Langmuir*, 2016, **32**, 4194-4202.
40. M. Amer and C. C. Wang, *Renew. Sust. Energ. Rev.*, 2017, **73**, 53-74.
41. S. Jacob, S. Pandey, J. D. Moral, A. Karimzadeh, J. Gil-Rostra, A. R. González-Elipe, A. Borrás and A. Winkler, *Adv. Mater. Technol.*, 2023, **8**, 2300263.
42. J. T. Luo, N. R. Geraldi, J. H. Guan, G. McHale, G. G. Wells and Y. Q. Fu, *Phys. Rev. Appl.*, 2017, **7**, 014017.
43. L. Y. Yeo and J. R. Friend, *Annu. Rev. Fluid Mech.*, 2014, **46**, 379-406.
44. C. Campbell, *Surface acoustic wave devices and their signal processing applications*, Elsevier, 2012.
45. F. Guo, Z. Mao, Y. Chen, Z. Xie, J. P. Lata, P. Li, L. Ren, J. Liu, J. Yang and M. Dao, *Proc. Natl. Acad. Sci. U.S.A.*, 2016, **113**, 1522-1527.
46. M. T. Rahni, A. S. Taleghani, M. Sheikholeslam and G. Ahmadi, *Wave Motion*, 2022, **111**, 102867.
47. B. Wiltshire, K. Mirshahidi, K. Golovin and M. H. Zarifi, *Sens. Actuators, B* 2019, **301**, 126881.
48. E. Madi, K. Pope, W. M. Huang and T. Iqbal, *Renew. Sust. Energ. Rev.*, 2019, **103**, 269-281.
49. Y. Chung, S. I. Na, J. Choi and M. S. Kim, *Appl. Therm. Eng.*, 2019, **155**, 461-469.
50. M. J. Song and C. B. Dang, *Int. J. Heat Mass Transf.*, 2018, **124**, 586-614.
51. Z. Yang, S. Rupavatharam, A. Burns, D. Lee, R. Howard and V. Isler, 2024.
52. L.-h. Zhang, J. Zhang, H.-w. Li and Q. Hu, 2012.
53. A. Lundberg, D. Gustafsson, C. Stumpp, B. Kløve and J. Feiccabrino, *Hydrology*, 2016, **3**, 28.
54. Y. C. Shen and X. F. Wang, *Int. J. Heat Mass Transf.*, 2019, **134**, 1171-1179.
55. Y. C. Shen and S. Wang, *Int. J. Heat Mass Transf.*, 2020, **147**, 118968.
56. M. J. Inanlu, Y. Gurumukhi, P. Kabirzadeh, R. Anand, S. Khodakarami, V. Viswanathan, A. Stillwell and N. Miljkovic, *Int. J. Heat Mass Transf.*, 2024, **225**, 125377.
57. M. X. Ou, M. Wang, J. Y. Zhang, Y. Y. Gu, W. D. Jia and S. Q. Dai, *Comput. Electron. Agric.*, 2024, **218**, 108743.
58. Y. C. Shen, H. Y. Zou and S. P. Wang, *Int. J. Heat Mass Transf.*, 2023, **217**, 124650.
59. D. Monga, Z. Guo, L. Shan, S. A. Taba, J. Sarma and X. Dai, *ACS Appl. Mater. Interfaces*, 2022, **14**, 13932-13941.
60. C. Furmidge, *J. Colloid Sci.*, 1962, **17**, 309-324.
61. M. J. Song, L. Xia, N. Mao and S. M. Deng, *Appl. Energy* 2016, **164**, 36-44.

Competing interests

Supplementary Information, including one PDF document and seven video files, is available.

The authors declare no competing interests.

Acknowledgement

Y.S. and X.D. acknowledge the DARPA Young Faculty Award (Award No. D23AP00160). F.C. and X.D. acknowledge the funding support by the National Institutes of Health (Award No. 1R03AI175720-01). M.H. and X.D. acknowledge funding support by the Department of Energy (Award No. DE-EE0011217). X.D. acknowledges the National Science Foundation Faculty Early Career Development Program (Award No. 2044348). D.B. acknowledges support from the U.S. Department of Energy Innovation in Buildings (IBUILD) Graduate Research Fellowship (Contract No. DE-AC05-00OR22725 and DE-SC0014664).

Author contributions

X.D. conceived and supervised the research. Y.S. and X.D. designed the experiments and analyzed the data. D. B. and F.G. designed the SAW actuator and Y.S. designed the capacitive sensor. D.B. and F.C. fabricated the coating and the device. Y.S. and M.H. carried out the experimental demonstration. Y.S., D.B., F.C. and X.D. wrote the manuscript. All authors revised the manuscript.

Supplementary Information, including one PDF document and seven video files, is available.

The data that support the findings of this study are available from the corresponding author upon reasonable request.